ARCHIVE OF MECHANICAL ENGINEERING

DOI: 10.24425/ame.2026.158902 2026, Vol. 73, No. 2, pp. 375–403

Abir LAMARI [1 2], Hicham BOUROUINA [1 2], Soumia KHOUNI [1 2],
Lamine ELAIHAR [1]

Coupling surface potential-based adatom-induced nonlocal vibration of a double resonator with an elastic medium under non-uniform thermal intensity

Received 31 August 2025, **Revised** 23 January 2026, **Accepted** 11 March 2026, **Published online** 11 June 2026

Keywords: adatom-resonator system, Hollow FGP sandwich, nonlocal strain gradient elasticity, Buckingham-Coulomb potential, nonlinear thermal load, differential quadrature method

The vibration behavior of an adatom-microresonator featuring a perforated microcore is examined in this paper. The nonlocal strain gradient theory (NSGT) is incorporated to characterize the microscale response. The system is subjected to a nonlinear thermal field and the adsorption of adatoms. The thermal response is modeled by solving a nonlinear steady-state heat conduction equation. Atom-surface interactions are characterized using the Buckingham-Coulomb interatomic potential. Furthermore, the model introduces the coupled dynamic behavior between the two functionally graded porous sandwich (FGPS) microbeams through a defined coupling stiffness term included in the governing equations. To evaluate the impact of rotary inertia, both the Rayleigh beam model (RBM) and the Euler-Bernoulli beam model (EBM) are employed, enabling a comparative analysis. The nonlocal frequencies are calculated using the Navier-type solution method (NTM) and the differential quadrature method (DQM). These frequency results are subsequently visualized through 3D numerical plots. A detailed analysis is performed to investigate the impact of physical parameters such as thermal gradients, porosity distribution, hole number, and adatom density on the nonlocal frequency shift of the system. The findings of this research are significant for advancing the fields of thermal monitoring and gas detection technologies.

✉ Hicham BOUROUINA, e-mail: bourouina.hicham@ens-bousaada.dz
[1] Physical Sciences Department, Higher Normal School of Bou-Saada, Msila, Algeria
[2] Laboratory of Physics of Materials and its Applications, University of Msila, Algeria

1. Introduction

Recent studies have examined improving the design and fabrication of double structures to enhance material performance for diverse sensing applications [1]. The double microbeam system, widely applied in MEMS [2], consists of two parallel beams interconnected by an elastic medium, allowing for intricate vibrational coupling [3]. To analyze bending and deflection, the Euler-Bernoulli beam model (EBM) is frequently used [4], while the Rayleigh beam model (RBM), which considers the rotatory inertia, offers improved insights into frequency behavior [5]. Together, these models enhance the understanding of vibration patterns and mechanical stability. For slender beams, the EBM and RBM are sufficient, as they assume shear deformation is negligible and bending dominates, making the switch to the Timoshenko beam model (TBM) produce almost no difference in deflection or natural frequency predictions [6, 7]. However, for less slender beams or thicker beams, shear deformation contributes noticeably to the overall stiffness, and in such cases, the TBM provides more accurate predictions of deflections and vibration frequencies by accounting for both shear and rotational effects [8, 9]. Recent investigations have extended this framework to double Rayleigh beams subjected to dynamic conditions such as moving and axial loads, leading to more refined theoretical developments [10]. Additionally, studies on double Euler beams have applied analytical, numerical, and approximate techniques to explore dynamic vibrations under different loads [11]. Liu et al. [12] assessed the vibrations of hybrid double beams coupled through a spring and subjected to axial force. Their research provides valuable insights that could pave the way for new engineering applications of double beam systems, revealing unique dynamic responses that do not appear in single beams.

Emerging trends in manufacturing technology innovation have permitted the production of functionally graded materials (FGMs), which exhibit a smooth transition between two material phases along specific directions [13]. Hemmatnezhad and Javid [14] conducted a study analyzing the free vibration of FG beams using a numerical method. Avcar and Alwan [15] derived the governing equations for FG Rayleigh beams, showing that variations in material properties have a significant impact on vibration frequencies. An important development in FGMs is the incorporation of porosity, which modifies their mechanical characteristics and overall structure, thereby affecting their vibrational response. Hung et al. [16] developed a porosity-dependent model, which was used to represent a linear relationship between the porosity coefficient and the material characteristics of sandwich beams that consist of an FGP core. Baghdali et al. [17] investigated the dynamic performance of FGP nanostructures and analyzed three types of porosity in their study. Arefi et al. [18] examined the response of a sandwich nanoplate composed of an FGP core under applied electric and magnetic potentials. The investigation analyzed the influence of the porosity coefficient, thermal parameters, and electric/magnetic potentials on bending, electrical, and magnetic responses of the system. Elaikh et al. [6] analyzed the vibration of FG Rayleigh beams with simple conditions. Their findings revealed that an elevation in the porosity index results in a decrease in the natural frequencies.

The addition of the perforation process to the microdevices' structure makes them useful by reducing total weight while maintaining structural stiffness [19]. Abdelrahman and Eltaher [20] investigated the bending of perforated nanobeams by integrating surface energy impacts within various beam theory frameworks. Civalek et al. [21] investigated the nonlinear stability of perforated nano/microbeams, utilizing nonlocal strain gradient theory and Fourier series, while considering the influence of an elastic medium. Mektout et al. [8] studied the resonance frequency of an FGP sandwich beam that consists of perforated cores. Lamari and Bourouina [22] investigated the vibration of a double FGPS microbeam featuring a two-dimensional square hole design, considering elastic coupling effects. Kafkas [23] focused on how structural parameters, such as the perforation parameters, affect the vibrational response of a perforated RBM.

The nonlocal strain gradient elasticity theory (NSGT) has established itself as a core theoretical approach for accurately modeling the mechanical response of micro- and nanoscale beams. By incorporating size effects and material microstructure [24], NSGT enables accurate modeling of structural responses, making it indispensable for MEMS/NEMS applications. Based on the NSGT, Zenkour and Radwan [25] studied the nonlocal vibration, bending, and stability of FGP nanobeams. Abdelrahman et al. [26] studied a finite element model incorporating NSGT to analyze the vibration of hollow nanobeams subjected to a dynamic force. Sourani et al. [27] analyzed the vibrational response of an EBM nanobeam subjected to external excitations, comparing their effectiveness within the framework of NSGT while accounting for surface effects. Guerroudj et al. [28] examined the dynamic behavior of FG nanobeams coated with a protective layer. Their study provided the influence of porosity ratio and nonlocal parameters on dynamic frequency characteristics. Collectively, these research efforts have highlighted the significance of NSGT in capturing microstructural effects in small-scale beams [29].

To solve the governing differential equations of double microbeam systems, a range of numerical and analytical methods has been employed. Bensaid et al. [30] studied the natural frequencies of hollow beams and solved the governing equations using the DQM, which was integrated with the finite element method. Feri et al. [31] employed the DQM to investigate the static and free vibration responses of cross-ply laminated composite plates. Karimi and Shahidi [32] investigated the influence of surface energy stresses on the bending and buckling behavior of a double-layer nanoplate. The governing equations were solved using the Galerkin method and validated through comparison with results obtained from Navier's method. Selvamani et al. [33] performed a study on the vibration of an FG nanobeam under the thermo-magneto-electric effect. The governing equations of motion were derived using Hamilton's principle and subsequently solved employing the NTM as an analytical approach. Nguyen et al. [34] studied the static performances of

FG plates, and the analytical solution was determined using NTS under simply supported boundary conditions. Bourouina et al. [35] applied the NTM to resolve deformation-deflection equations, underscoring its relevance in nonlocal elasticity studies [36]. Ultimately, combining DQM and NTM improves computational efficiency, enhances predictive modeling, and broadens the nonlocal elasticity within mechanics [37].

Surface effects are known to significantly impact resonance behavior, especially those arising from mass adsorption [38]. Bourouina and Boussendel [39] investigated the role of hydrogen bonding and van der Waals (vdW) interactions in the nonlocal dynamics of molecule-resonator biosensors. Zhang et al. [40] proposed a model for predicting microcantilever bending responses caused by adatoms. A range of interaction potentials has been employed to explore the interfacial dynamics between adsorbates and microbeam surfaces [37]. The Buckingham-Coulomb potential is an interatomic potential particularly well-suited for modeling ionic systems [41]. Shukla et al. [42] employed a Coulomb potential combined with a standard Buckingham potential to characterize the interactions between constituent ions. Lamari et al. [7] used the Lennard-Jones (6-12), Morse, and Buckingham potentials to model the interaction energies between the adatoms and the effective surface atoms in the double FGPS microresonator. The Buckingham potential was employed to examine the interactions between water molecules and silica surfaces, providing the molecular mechanisms underlying water performance at the solid-liquid interface [43]. These findings are essential for enhancing the efficiency of kinetics and for guiding the advanced micro-scale sensing devices.

Microbeam systems demonstrate vibrational characteristics that can be substantially affected by external variables, including temperature loads. Chen et al. [44] investigated the buckling of an FG beam under thermal effects. The temperature was considered both uniform and variable along the thickness direction. Esen [9] investigated the effects of a moving mass on the transverse and axial dynamic behavior of FGM beams in a thermal medium, converting thermal stresses into mechanical equivalents and including them in the stiffness matrix. Abdelbari et al. [45] studied the influence of different thermal loads on the vibrational response of FGP beams resting on foundations, assuming that the thermal characteristics vary smoothly along the thickness direction. Rahmani et al. [46] developed a theoretical model for microsensors in which the dynamic behavior of an Euler beam was investigated under different temperature rises. Salari et al. [47] examined the nonlinear thermal bending and buckling of FGP beams subjected to lateral mechanical loading. Their analysis considered two thermal conditions: transverse heat conduction and a uniform temperature rise.

This study focuses on evaluating the vibrational characteristics of double FGP microresonators featuring a hollow microlayer under the coupled effects of surface adsorption phenomena and nonlinear thermal field. An integrated approach based on the NSGT, EBM formulation, and RBM is employed to investigate the influence of nanoscale interactions and spatially distributed oxygen charge on the variation of the system's nonlocal frequency. The integration of nonlocal elasticity theory with numerical methods like DQM offers a computationally efficient alternative to conventional lattice dynamics approaches, which often involve solving intricate coupled integral systems. Attention is also given to the impact of perforation geometry, and structural features on the equivalent properties of the double FGP microresonators. The modeling begins in Section 2 with a characterization of the microstructure under thermal gradients, detailing effective material properties and governing factors. The energy of vdW interactions is computed using the Buckingham-Coulomb potential. Section 3 formulates the dynamic equations for the system using beam theory within an NSGT framework, resulting in a set of coupled equations. Analytical and numerical approaches, including the NTM and DQM, are then employed to determine the nonlocal frequencies in Section 4. In particular, the DQM is recognized for its high computational accuracy and effectiveness in handling intricate boundary conditions, whereas the NTM offers a robust analytical framework for analyzing vibrational characteristics. Section 5 presents a detailed parametric study examining the influence of material gradation, porosity, adsorption phenomena, spring stiffness, the nonlocal parameter, and the nonlinear thermal environment, followed by a validation against a previous study. The main conclusions and key observations are focused on in Section 6.

2. Adatom-microresonator system design

This section presents a refined analytical model for an adatom-functionalized resonator operating under thermal conditions. The adsorption energy is determined based on the derived interaction potential. The model considers the influence of temperature, uniformly distributed porosity, and perforation parameters on the system's nonlocal dynamic response.

2.1. Integrated microstructural configuration

An adatom-functionalized microresonator system comprises two FGPS microbeams, connected by an elastic layer. Both FGPS microbeams have a hollow microcore and identical geometric properties, including width b, thickness h, and length L, as represented in Fig. 1.

Consider an FGPS microbeam with a porosity volume fraction ζ, assuming an even distribution across the thickness. According to the modified rule of mixture, the total volume fractions of metal and ceramic satisfy $V_m + V_C = 1$, and the ceramic volume fraction follows the power-law distribution $V_c = (z/h + 1/2)^p$ [48]. Based on this formulation, the effective material properties under a temperature change T, Young's modulus E, thermal conductivity κ, and thermal expansion coefficient λ,

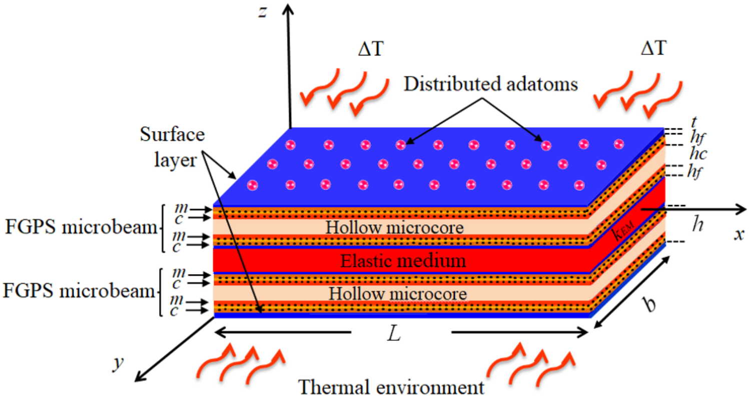

Fig. 1. Illustration of a double microresonator system subjected to distributed adatom and thermal field

are expressed as follows [9, 36]:

$$E(z,T) = E_m(T) + \left(E_c(T) - E_m(T)\right)\left(\frac{1}{2} + \frac{z}{h}\right)^p - \frac{\zeta}{2}\left(E_c(T) + E_m(T)\right), \tag{1}$$

$$\kappa(z,T) = \kappa_m(T) + \left(\kappa_c(T) - \kappa_m(T)\right)\left(\frac{1}{2} + \frac{z}{h}\right)^p - \frac{\zeta}{2}\left(\kappa_c(T) + \kappa_m(T)\right), \tag{2}$$

$$\lambda(z,T) = \lambda_m(T) + \left(\lambda_c(T) - \lambda_m(T)\right)\left(\frac{1}{2} + \frac{z}{h}\right)^p - \frac{\zeta}{2}\left(\lambda_c(T) + \lambda_m(T)\right), \tag{3}$$

where the variable z ranges over the upper and lower face layers, defined by the interval:

$$z \in \left[-\frac{h_c}{2} - h_f,\ \frac{h_c}{2} + h_f\right]. \tag{4}$$

The indices m and c correspond to the metallic and ceramic layers, respectively. It is important to note that the positive real parameter p $(0 \leq p < \infty)$ represents the power-law index. When $p = 0$, the FGPS microbeam behaves as a fully ceramic structure, whereas very large values of p result in an almost entirely metallic beam [48]. In these formulations, the first term describes the smooth gradation between the ceramic and metal constituents and depends on the power-law index p. In contrast, the second term is independent of the power-law index p and describes the even distribution of porosity [22].

The terms h_f and h_c denote the thicknesses of the face and core layers, respectively. Under thermal loading conditions, the material density ρ is considered temperature-independent [18]:

$$\rho(z) = \rho_m + (\rho_c - \rho_m)\left(\frac{1}{2} + \frac{z}{h}\right)^p - \frac{\zeta}{2}(\rho_c + \rho_m) \quad z \in \left[-\frac{h_c}{2} - h_f,\ \frac{h_c}{2} + h_f\right]. \tag{5}$$

While the thermal conductivity κ_c and thermal expansion coefficient λ_c are assumed to remain constant throughout the hollow microcore [9], the mechanical properties, namely the Young's modulus E_{mc} and the density ρ_{mc}, are directly influenced by the perforation geometry of the hollow microcore. According to Luschi and Pieri [49]:

$$\begin{aligned} E_{mc}(z,T) &= (1-\alpha)E_c(T) = \left(1-\frac{l_h}{l_p}\right)E_c(T) = \left(\frac{L-l_hN}{L}\right)E_c(T) \\ &= \left(\frac{l_pN-l_hN}{L}\right)E_c(T) = \left[\frac{(l_p-l_h)N}{L}\right]E_c(T) \quad z\in\left[-\frac{h_c}{2},\frac{h_c}{2}\right], \end{aligned} \tag{6}$$

$$\begin{aligned} \rho_{mc}(z) &= (1-\alpha)(2-(1-\alpha))\rho_c(z) = \left(1-\frac{l_h}{l_p}\right)\left(2-\left(1-\frac{l_h}{l_p}\right)\right)\rho_c(z) \\ &= \frac{(l_p-l_h)N}{L}\left[2-\frac{(l_p-l_h)N}{L}\right]\rho_c(z) \qquad z\in\left[-\frac{h_c}{2},\frac{h_c}{2}\right]. \end{aligned} \tag{7}$$

Here, L denotes the length of the hollow microcore, and l_h the difference between two successive hole sizes. We define N as the number of hole cells along the hollow microcore, which generates a periodic square holes network with a spatial period $l_p = L/N$ [49, 50]. The relation between l_h and l_p is expressed by the parameter α ($\alpha = l_h/l_p$, known as the filling ratio [49].

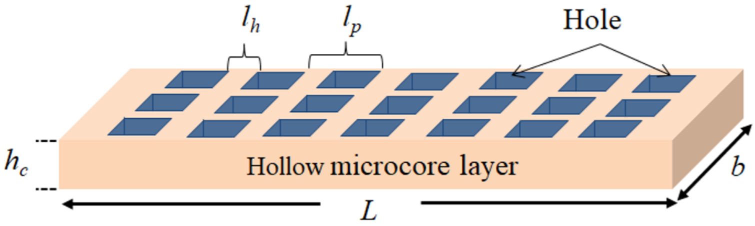

Fig. 2. Hollow microcore layer with a two-dimensional square holes network

Furthermore, the closed-form formulations of the equivalent bending rigidity EI_{eq}, equivalent mass per unit length ρA_{eq}, and equivalent rotary inertia per unit length ρI_{eq} are computed by Lamari et al. [7]:

$$EI_{\text{eq}} = \int_A E(z,T)z^2\,\mathrm{d}A, \tag{8a}$$

$$\rho A_{\text{eq}} = \int_A \rho(z)\,\mathrm{d}A, \tag{8b}$$

$$\rho I_{\text{eq}} = \int_A \rho(z)z^2\,\mathrm{d}A. \tag{8c}$$

The term I represents the second moment ($I = bh^3/12$), and $A = bh$ is the section of the microbeam's area. The presented equations illustrate the impact of material property variations across the layers of the double FGPS microresonator on its equivalent parameters.

2.2. Nonlinear thermal load

This section considers a thermal boundary condition where distinct temperature values are applied to the upper and lower surfaces. Under this assumption, the transverse temperature gradient is defined by solving the stationary heat conduction equation. The governing equation for the transverse temperature variation is expressed as [9]:

$$-\frac{d}{dz}\left(\kappa(z,T)\frac{dT}{dz}\right) = 0. \tag{9}$$

The resulting solution to the temperature distribution equation is formulated as:

$$T(z) = T_0 + \Delta T(z), \tag{10}$$

where T_0 is the ambient or free stress temperature, ΔT denotes the temperature change [46]. The temperature variation across the thickness direction z is evaluated to capture the thermal gradient within the microresonator [46]:

$$T(z) = T_m + \frac{(T_c - T_m)}{\displaystyle\int_{-h/2}^{h/2} \frac{1}{\kappa(z,T)}\,\mathrm{d}z} \int_{-h/2}^{z} \frac{1}{\kappa(z,T)}\,\mathrm{d}z. \tag{11}$$

Under this type of thermal loading, the one-dimensional steady-state heat conduction equation (Eq. (9)) is solved to determine the temperature distribution of the double FGPS microbeams system.

2.3. Modeling adsorption phenomena

This section investigates the vdW interactions between adsorbed atoms and their surrounding atomic environment within the adatom-microresonator system. The interaction energy between atom pairs i and j is modeled using the Coulomb potential supplemented by a standard Buckingham potential [42]:

$$u_{BC}^{\mathrm{vdW}}(r_{ij}) = \mathrm{A}e^{-(r_{ij}/\varepsilon)} - \frac{C}{r_{ij}^6} + \frac{1}{4\pi\varepsilon_0}\frac{q_i q_j}{r_{ij}}, \tag{12}$$

where A denotes the repulsion energy coefficient, C is the dispersion attraction coefficient, and ε is the decay length Buckingham [7]. The first term is the Buckingham potential, and the second term is the Coulomb potential [42]. The terms q_i

and q_j are partial or full charges on atoms, with the formal charges, ε_0 represents vacuum permittivity, and r_{ij} is the interatomic distance [22]. In this model, silicon (Si) atoms are still used on the microbeam surface, but these surface Si atoms can behave like partially charged Si^{4+} due to interaction with adsorbed oxygen (O^{2-}). The vdW interaction energy between an adatom and specific atoms within the system, such as interactions between adatom P and atom 1 or adatom Q and atom 3 (Fig. 3b), is expressed as follows [7]:

$$u_{Q3}^{BC} = u_{P1}^{BC} = \mathrm{A}e^{-\left(\frac{r_{P1}}{\varepsilon}\right)} - \frac{C}{r_{P1}^6} + \frac{1}{4\pi\varepsilon_0}\frac{q_P q_1}{r_{P1}}, \tag{13}$$

where $r_{P1} = r_{Q3}$ represents the distance between an adatom p and a double FGPS microresonator atom 1 [35]. During bending, the distance between two neighboring adatoms P and Q changes to $r_{PQ} = d + e$.

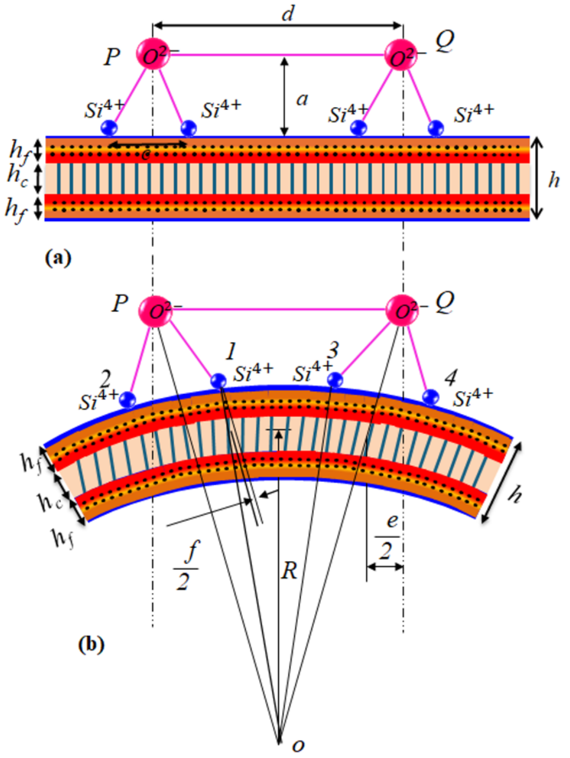

Fig. 3. Deformation of the adatom-microresonator system: (a) equilibrium state, (b) after distributing the oxygen charge

The vdW interaction energy between adatoms P and Q can be expressed using the deformed distance r_{PQ} in Eq. (12). The adsorption density η determines the spacing d between adjacent adatoms, following the relation $d^2 = 1/\eta$. The modified vdW interaction energy per unit area for the adatom-microresonator system is defined as [22]:

$$u_{\mathrm{int}}^{BC} = \left(2u_{P1}^{BC} + u_{PQ}^{BC}\right). \tag{14}$$

The potential energy of interaction between the adatoms and the microresonator system, denoted as U_{Pa}, corresponds to the total interaction energy U_{int}, reflecting the physical coupling at the nanoscale U_{int} [19]:

$$(U_{\mathrm{int}})_{BC} = b\int_0^L u_{\mathrm{int}}^{BC}\,\mathrm{d}x. \tag{15}$$

Based on the Taylor series expansion, the interaction energy can be effectively approximated by retaining the first three terms of the expansion around the reference configuration [22]. Accordingly, Eq. (14) is reformulated as follows:

$$(U_{\mathrm{int}})_{BC} = b\int_0^L \left(u_0^{BC} + \varphi^{BC}\,\mathrm{K} + \frac{1}{2}\phi^{BC}\,\mathrm{K}^2\right)\mathrm{d}x. \tag{16}$$

Here K is related to the transverse deflection w by $\mathrm{K} = \partial^2 w/\partial x^2$ [51]. The terms: u^{BC}, φ^{BC}, and ϕ^{BC} are computed using the Buckingham-Coulomb interaction u^{BC}, where $\varphi^{BC} = \partial u_{\mathrm{int}}^{BC}/\partial\mathrm{K}\big|_{\mathrm{K}=0}$, and $\phi^{BC} = \partial^2 u_{\mathrm{int}}^{BC}/\partial\mathrm{K}^2\big|_{\mathrm{K}=0}$ [35]. This Buckingham-Coulomb potential is particularly relevant for ionic or partially ionic systems, like adatom-functionalized microresonators involving charged adsorbed species.

3. Integrated framework for dynamic response

This section presents a mathematical model based on the NSGT to analyze the bending behavior of a simply supported microresonator. By incorporating EBM and RBM, the model enables an evaluation of the system's nonlocal resonance frequencies.

3.1. Nonlocal strain gradient-enhanced elastic behavior

In the NSGT, both nonlocal softening and strain gradient stiffening effects are incorporated simultaneously. The total stress tensor is obtained by combining the classical and higher-order stress components as [26]:

$$t = \boldsymbol{\sigma} - \nabla\cdot\boldsymbol{\sigma}^{(1)}, \tag{17}$$

where σ and $\sigma^{(1)}$ represent the classical and higher-order stress tensors. By introducing linear differential operators, the constitutive relation for the axial stress distribution can be expressed in the simplified form [7]:

$$t_{xx} - (ea)^2 \frac{\partial^2 t_{xx}}{\partial x^2} = E\varepsilon_{xx} - El^2 \frac{\partial^2 \varepsilon_{xx}}{\partial x^2}\,. \tag{18}$$

Finally, applying NSGT to the FGPS microbeam cross-section leads to the governing bending relation [31]:

$$\left(1 - (ea)^2 \frac{\partial^2}{\partial x^2}\right) M = -EI^* \left(1 - l^2 \frac{\partial^2}{\partial x^2}\right) \frac{\partial^2 w(x,t)}{\partial x^2}\,, \tag{19}$$

where M denotes the moment resultant of the total stress, and the effective bending stiffness of the adatom-microresonator is represented as EI^* [35]. The terms l and ea represent the nonlocal and strain gradient length scale parameters, respectively [31].

3.2. Fundamental equations governing dynamic vibration

This section enhances the fundamental dynamic equation by integrating axial effects into the Lagrangian formulation of an FGPS microresonator featuring a hollow core, while also considering the influence of adsorption phenomena. The interaction between adatoms and the microstructure is incorporated to evaluate its effect on the system's stability and vibrational behavior. As a result, the system's total potential energy [37] is formulated as:

$$\Pi = U_b + U_{\mathrm{int}}\,, \tag{20}$$

where the total elastic strain energy of the bending behavior of an FGPS microresonator is represented by [37]:

$$U_b = \frac{1}{2} EI \int_0^L \kappa^2 \mathrm{d}x. \tag{21}$$

The kinetic energy expression for the hollow FGPS microresonator is formulated as [22, 35]:

$$T = \frac{1}{2} \int_0^L \left(\rho A_{\mathrm{eq}} + \eta b m_{O^-}\right) \left(\frac{\partial w(x,t)}{\partial t}\right)^2 \mathrm{d}x + \frac{1}{2} \int_0^L \rho I_{\mathrm{eq}} \left(\frac{\partial^2 w(x,t)}{\partial x \partial t}\right)^2 \mathrm{d}x. \tag{22}$$

The parameter $\eta = 1/d^2_{O^- - O^-}$ represents the distribution density, d denotes the distance between two adatoms, and m_{O^-} the mass of adatoms, respectively. The surface potential energy [52] is given:

$$U_s = \int_0^L p(x) w\, \mathrm{d}x. \tag{23}$$

In this context, $p(x) = HK$ represents the transverse load induced by the residual surface stress τ_0 in the deformed microbeam, where $H = 2\tau_0 b$ [52]. By applying the Hamilton's principle, function $L = T - (\Pi - U_s)$, with the Lagrangian function defined as $\delta \int L \, \mathrm{d}t = 0$, the governing moment equation for the EBM is obtained.

$$\begin{aligned}\frac{\partial^2 M}{\partial x^2} - \left(\rho A_{\text{eq}} + \eta b m_{O^-}\right) \frac{\partial^2 w(x,t)}{\partial t^2} - \eta b \phi^{BC} \frac{\partial^4 w}{\partial x^4} \\ = -HK - Q(x,t) - F_T \frac{\partial^2 w}{\partial x^2} \,,\end{aligned} \tag{24}$$

$$F_T = -\int_A E(z,T)\alpha(z,T)\Delta T(z)\,\mathrm{d}A, \tag{25}$$

where, F_T represents the nonlinear thermal load [47] and Q is the transverse load [22]. According to Eq. (19) and based on the NSGT, the nonlocal bending moment equation of EBM can be expressed as [7]:

$$M = (ea)^2 \frac{\partial^2 M}{\partial x^2} - EI^* \left(1 - l^2 \frac{\partial^2}{\partial x^2}\right) \frac{\partial^2 w(x,t)}{\partial x^2} \,. \tag{26}$$

Substituting Eq. (19) into Eq. (26) produces the nonlocal formulation for the bending moment M in an adatom-microresonator featuring a hollow microcore:

$$\begin{aligned}M = -EI^* \left(1 - l^2 \frac{\partial^2}{\partial x^2}\right) \frac{\partial^2 w(x,t)}{\partial x^2} + (ea)^2 \Bigg[\left(\rho A_{\text{eq}} + \eta b m_{O^-}\right) \frac{\partial^2 w(x,t)}{\partial t^2} \\ + \eta b \phi^{BC} \frac{\partial^4 w(x,t)}{\partial x^4} - 2\tau_0 b \frac{\partial^2 w(x,t)}{\partial x^2} - Q(x,t) - F_T \frac{\partial^2 w(x,t)}{\partial x^2} \Bigg] .\end{aligned} \tag{27}$$

The EBM governing equation in small-scale under oxygen charge distribution and nonlinear thermal load is given by the following equation:

$$\begin{aligned}EI^* \left(1 - l^2 \frac{\partial^2}{\partial x^2}\right) \frac{\partial^4 w(x,t)}{\partial x^4} + \left(1 - (ea)^2 \frac{\partial^2}{\partial x^2}\right) \Bigg[\left(\rho A_{\text{eq}} + \eta b m_{O^-}\right) \frac{\partial^2 w(x,t)}{\partial t^2} \\ + \eta b \phi^{BC} \frac{\partial^4 w(x,t)}{\partial x^4} - \left(2\tau_0 b + F_T\right) \frac{\partial^2 w(x,t)}{\partial x^2} - Q(x,t) \Bigg] = 0\end{aligned} \tag{28}$$

To obtain the RBM equation, the effects of rotary inertia are incorporated in the EBM equation via the introduction of a term containing the second derivative of the displacement with respect to x:

$$\begin{aligned}\frac{\partial^2 M}{\partial x^2} - \left(\rho A_{\text{eq}} + \eta b m_{O^-}\right) \frac{\partial^2 w(x,t)}{\partial t^2} - \eta b \phi^{BC} \frac{\partial^4 w}{\partial x^4} - \rho I_{\text{eq}} \frac{\partial^4 w(x,t)}{\partial x^2 \partial t^2} \\ = -HK - Q(x,t) - F_T \frac{\partial^2 w}{\partial x^2} \,.\end{aligned} \tag{29}$$

The additional term $(\rho I_{\text{eq}}\partial^4 w(x,t)/\partial x^2\partial t^2)$ accounts for the rotatory inertia impact. The RBM governing equations, incorporating nonlocal effect, nonlinear thermal load, and distributed oxygen charge, are formulated as follows:

$$
\begin{aligned}
EI^{*}\left(1-l^{2}\frac{\partial^{2}}{\partial x^{2}}\right)\frac{\partial^{4}w(x,t)}{\partial x^{4}}+\left(1-(ea)^{2}\frac{\partial^{2}}{\partial x^{2}}\right)\Bigg[\left(\rho A_{\text{eq}}+\eta b m_{O^{-}}\right)\frac{\partial^{2}w(x,t)}{\partial t^{2}}\\
+\ \eta b\phi^{BC}\frac{\partial^{4}w(x,t)}{\partial x^{4}}-\left(2\tau_{0}b+F_{T}\right)\frac{\partial^{2}w(x,t)}{\partial x^{2}}\\
+\rho I_{\text{eq}}\frac{\partial^{4}w(x,t)}{\partial x^{2}\partial t^{2}}-Q(x,t)\Bigg]=0.
\end{aligned}
\tag{30}
$$

Eqs. (28) and (29) provide the EBM and RBM nonlocal vibration equations, respectively. It is worth noting that the effect of the transverse load Q was not considered in the dynamic vibration model proposed by Bourouina et al. [11].

4. Modeling nonlocal dynamic vibration modeling

This section examines the nonlocal frequency influenced by adsorption. In the context of small deformations, simply-supported microbeams are commonly employed in the design of microresonators. The nonlocal dynamic equation, initially formulated for a single FGPS microbeam containing a hollow core, is developed to assess the dynamic response of a double FGPS microresonator. Resonance frequencies are determined using two complementary approaches: the analytical NTM and the numerical DQM approach.

4.1. Nonlocal coupled motion equations

To evaluate the nonlocal performance resulting from the coupling with the elastic layer, the vibration behavior of a functional microresonator system is investigated by the NSGT inside the frameworks of the RBM and the EBM, which accounts for both spring stiffness effects and bending behavior. The equations of motion [22] are formulated separately for two configurations:

Single FGPS microresonator {1}

$$
\begin{aligned}
EI_{1}^{*}\left(1-l^{2}\frac{\partial^{2}}{\partial x^{2}}\right)\frac{\partial^{4}w_{1}(x,t)}{\partial x^{4}}+k_{EM}\left[w_{1}(x,t)-w_{2}(x,t)\right]\\
-\ (ea)^{2}k_{EM}\frac{\partial^{2}}{\partial x^{2}}\left[w_{1}(x,t)-w_{2}(x,t)\right]\\
+\ \left(1-(ea)^{2}\frac{\partial^{2}}{\partial x^{2}}\right)\Bigg[\left(\rho A_{\text{eq}1}+\eta b m_{O^{-}}\right)\frac{\partial^{2}w_{1}(x,t)}{\partial t^{2}}+\eta b\phi^{BC}\frac{\partial^{4}w_{1}(x,t)}{\partial x^{4}}\\
-\left(2\tau_{0}b+F_{T_1}\right)\frac{\partial^{2}w_{1}(x,t)}{\partial x^{2}}+\rho I_{\text{eq}1}\frac{\partial^{4}w_{1}(x,t)}{\partial x^{2}\partial t^{2}}\Bigg]=0.
\end{aligned}
\tag{31}
$$

Single FGPS microresonator {2}

$$
\begin{aligned}
&EI_1^*\left(1-l^2\frac{\partial^2}{\partial x^2}\right)\frac{\partial^4 w_2(x,t)}{\partial x^4}-k_{EM}\left[w_1(x,t)-w_2(x,t)\right]\\
&\quad+\ (ea)^2 k_{EM}\frac{\partial^2}{\partial x^2}\left[w_1(x,t)-w_2(x,t)\right]\\
&\quad+\left(1-(ea)^2\frac{\partial^2}{\partial x^2}\right)\left[\left(\rho A_{\mathrm{eq1}}+\eta b m_{O^-}\right)\frac{\partial^2 w_2(x,t)}{\partial t^2}+\eta b\phi^{BC}\frac{\partial^4 w_2(x,t)}{\partial x^4}\right.\\
&\quad-\ \left.\left(2\tau_0 b+F_{T_2}\right)\frac{\partial^2 w_2(x,t)}{\partial x^2}+\rho I_{\mathrm{eq2}}\frac{\partial^4 w_2(x,t)}{\partial x^2\partial t^2}\right]=0,
\end{aligned}
\tag{32}
$$

where k_{EM} represents the elastic medium parameter. The equivalent characteristics of single FGPS microresonator {1} and {2} are identical $EI_1^* = EI_2^* = EI^*$, $\rho A_{\mathrm{eq1}} = \rho A_{\mathrm{eq2}} = \rho A_{\mathrm{eq}}$, $\rho I_1 = \rho I_2 = \rho I_{\mathrm{eq}}$ [27]. Furthermore, both microbeams are exposed to an identical thermal load $FT_1 = FT_2 = F_T$. The dynamic deflection of the primary perforated microstructure is expressed as [39]:

$$
w_1(x,t)-w_2(x,t)=w(x,t). \tag{33}
$$

As previously discussed, the RBM equations, Eq. (31) and Eq. (32) can be rewritten by differentiating with respect to the spatial coordinate x. Substituting $\partial^2 w(x,t)/\partial t^2$ leads to the following time-domain equations of motion for the system based on RBM and EBM theories:

$$
\begin{aligned}
&C_1^R\frac{\partial^6 w(x,t)}{\partial x^6}+C_2^R\frac{\partial^4 w(x,t)}{\partial x^4}+C_3^R\frac{\partial^2 w(x,t)}{\partial x^2}-C_4^R\frac{\partial^4 w(x,t)}{\partial x^2\partial t^2}+C_5^R w(x,t)\\
&\quad+\frac{\partial^2 w(x,t)}{\partial t^2}+C_6^R\frac{\partial^4 w(x,t)}{\partial x^2\partial t^2}-C_7^R\frac{\partial^6 w(x,t)}{\partial x^4\partial t^2}=0.
\end{aligned}
\tag{34}
$$

Neglecting rotary inertia reduces the equation to the EBM formulation, which includes nonlocal effects, as presented below:

$$
\begin{aligned}
&C_1^E\frac{\partial^6 w(x,t)}{\partial x^6}+C_2^E\frac{\partial^4 w(x,t)}{\partial x^4}+C_3^E\frac{\partial^2 w(x,t)}{\partial x^2}-C_4^E\frac{\partial^4 w(x,t)}{\partial x^2\partial t^2}+C_5^E w(x,t)\\
&\quad+\frac{\partial^2 w(x,t)}{\partial t^2}=0.
\end{aligned}
\tag{35}
$$

The first five terms on the left-hand side of Eq. (34) are consistent with those in the EBM, while the additional terms account for the rotary inertia impact in the RBM. The terms C_R and C_E in Eq. (34) and Eq. (35) correspond to the RBM and EBM, respectively.

4.2. NTM solution approach

In this subsection, the NTM is used to solve the governing differential equations of the system, incorporating the effects of the NSGT under thermal loading. The double FGPS microresonator is represented as a simply supported structure to achieve the conditions required by the NTM framework [39]. This method enables the analytical derivation of nonlocal resonance frequencies. Under the assumption of small-amplitude vibrations, the transverse displacement is considered to take the form presented in [7]:

$$w(x,t) = \sum_{n=1}^{\infty} w_n \sin \lambda_n x e^{i\omega_n t}. \tag{36}$$

Here, w represents the flexural deflection amplitude, ω_n is the natural frequency (n-th mode pulsation), and $\lambda_n = n\pi/L$ denotes the wave number. By substituting Eq. (36) into Eqs. (34) and (35), the nonlocal resonance frequencies of the double FGPS microresonator are obtained for both the RBM and the EBM as follows:

$$\left(\omega_n^2\right)_{RBM} = \left(\omega_n^2\right)_{EBM} .\psi(n), \tag{37}$$

$$\begin{aligned} \left(\omega_n^2\right)_{EBM} &= \frac{-C_1^E \lambda_n^6 + C_2^E \lambda_n^4 - C_3^E \lambda_n^2 + C_5^E}{\left(1 - C_4^E \lambda_n^2\right)}, \\ \psi(n) &= \frac{1 + C_2^E \lambda_n^4}{\left(1 + C_4^E \lambda_n^2 - C_6^R \lambda_n^2 - C_7^R \lambda_n^4\right)}. \end{aligned} \tag{38}$$

These expressions account for bending deformation induced by adsorption effects, while also incorporating surface layer stress and nonlinear thermal load.

4.3. Numerical solution approach

To solve the differential equations, the efficient numerical solution method DQM was used, which is specifically valued for its exactness in handling complex partial differential equations (PDEs) with minimal computational cost. The method discretizes the study domain into m points, approximating function derivatives $f(x)$ as weighted linear sums of function values at all discretized points internal to the interval $[0, L]$. To improve computational efficiency and accuracy, the Gauss-Lobatto-Chebyshev distribution is employed for discretization as bellow [7, 53]:

$$\begin{aligned} &x_1 = 0, \qquad x_m = L, \\ &x_i = \frac{L}{2}\left[1 - \cos\left(\frac{i-1}{m-1}\pi\right)\right] \quad (i = 2, 3, \ldots, m-1). \end{aligned} \tag{39}$$

This numerical method is highly effective in approximating the derivatives of a displacement function by expressing them as a weighted linear integration of function values at discrete points within the domain [7]:

$$\left.\frac{d^r f}{dx^r}\right|_{x=x_i} = \sum_{j=1}^{m} A^r_{(ij)} f(x_j). \tag{40}$$

The coefficients $A^{(r)}$ serve as weighting factors, with m representing the total number of grid points and r denoting the derivative order. The first-order derivative expression is numerically approximated as outlined in [53]. For higher-order derivatives ($r = 2, 3, \ldots, m-1$), a repetition relation is employed to compute the corresponding derivatives efficiently. Fig. 4 illustrates the flowchart outlining the linear DQM analysis process for the double FGPS microresonator.

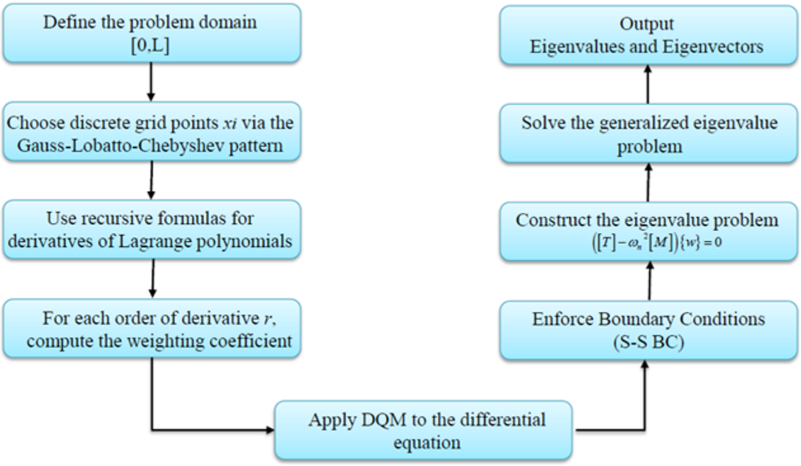

Fig. 4. Numerical technique flowchart used to compute the eigenvalues

To simplify, we used the symbols w_i and w_j. The Eqns. (34) and (35) of RBM and EBM become:

$$w(x_j, t) = w_j, \qquad w(x_i, t) = w_i\,, \tag{41}$$

$$\sum_{j=1}^{m}\left(C_1^R A_{ij}^{(6)} + C_2^R A_{ij}^{(4)} + C_3^R A_{ij}^{(2)}\right) w_j + C_5^R w_i + \omega_n^2\left(\sum_{j=1}^{N}\left(C_4^R A_{ij}^{(2)} - C_6^R A_{ij}^{(2)} + C_7^R A_{ij}^{(4)}\right) w_j - w_i\right) = 0, \tag{42}$$

$$\sum_{j=1}^{m}\left(C_1^E A_{ij}^{(6)} + C_2^E A_{ij}^{(4)} + C_3^E A_{ij}^{(2)}\right) w_j + C_5^E w_i + \omega_n^2\left(\sum_{j=1}^{N} C_4^E A_{ij}^{(2)} w_j - w_i\right) = 0. \tag{43}$$

The simply supported boundary conditions are used in this work as follows [7]:

$$x_i \in [0,\ L]; \quad w_1 = w_m = 0; \quad \sum_{j=1}^{m} A_{1j}^{(2)} w_j = \sum_{j=1}^{m} A_{mj}^{(2)} w_j = 0. \tag{44}$$

The equations of motion for both the RBM and EBM, using their associated boundary conditions and utilizing Eq. (43) and the modified weighting coefficient matrix [53], are represented in matrix form as follows:

$$\left([T] - \omega_n^2\,[M]\right)\{w\} = 0. \tag{45}$$

Here, $[T]$ represents the stiffness matrix, $[M]$ stands for the mass matrix, and $\{w\}$ corresponds to the deflection vector.

Eqs. (37) and (38) define an eigenvalue problem for both the EBM and RBM, which is solved numerically.

5. Numerical computation and discussions

First, this work performs a validation study for the proposed method. Then, the proven approach is applied to analyze the multiphysics parameters and the vibration response of the double FGPS microresonators under adatom distribution and thermal load. studied system has the materials chosen for the adatom-microresonator include single-crystal silicon (Si) with a density of $\rho_m = 2330$ kg/m^3, Young's modulus $E_m = 169$ GPa [7], thermal expansion coefficient $\lambda = 2.6 \cdot 10^{-6}$ K^{-1}, and thermal conductivity $\kappa = 150$ W/mK [54], silicon carbide ceramic (SiC) with a density of $\rho_c = 3210$ kg/m^3, Young's modulus $E_c = 420$ GPa [27], thermal expansion coefficient $\lambda = 3 \cdot 10^{-6}$ K^{-1} [54], and thermal conductivity $\kappa = 70$ W/mK [54] for the upper and lower layers. The hollow microcore consists of SiC (100) ceramic, while the added surface layer is from Si (100). The study focuses on simply supported double FGPS microresonators. MATLAB software was used for all the computations in this section.

5.1. Validation

To assess the accuracy of the proposed method, a comparative analysis is performed by referencing both analytical and numerical results from a prior study. Table 1 presents a comparison between the nonlocal frequencies obtained using the Buckingham potential, which evaluates the total interaction energy, and those derived from the Buckingham-Coulomb potential. To capture the adsorption behavior, the surface elastic constant $S = -0.76086$ eVÅ^{-2} [51] and the residual surface stress $\tau_0 = 1.4$ N/m [52] are incorporated into the theoretical model. Additionally, key parameters are considered, $a = 3.26$ Å represents the equilibrium displacement between an adatom and a surface atom, while $c = 3.43$ Å corresponds to the spacing between two Si atoms [35]. The dimensionless parameter, $\theta = \eta/\eta_m$, is introduced to characterize the adsorption density of distributed oxygen charge. Here, $\eta_m = 1/c^2$ serves as a reference density, ensuring that the impact of adatom distribution on the microbeam's response is appropriately captured [22].

Table 1. A comparison between the nonlocal frequencies [GHz] computed via the Buckingham and the Buckingham-Coulomb potentials versus the L/h ratio and power law index p, using the analytical and numerical methods

L/h ratio	Power law index p	NTM/DQM	Nonlocal frequency			
			ω^a_{Buk}		ω^a_{BC}	
			EBM [7]	RBM [7]	EBM [Present]	RBM [Present]
05	0	NTM	17.465721	17.354475	17.276887	17.276849
		DQM	17.465706	17.354451	17.276622	17.276592
	0.5	NTM	14.447622	14.433799	14.206845	14.206791
		DQM	14.447610	14.433764	14.206476	14.206644
	01	NTM	12.711938	12.591444	12.331443	12.331388
		DQM	12.711582	12.591417	12.331419	12.331359
10	0	NTM	15.364265	15.360812	15.157786	15.157739
		DQM	15.364223	15.360684	15.157637	15.157591
	0.5	NTM	12.583297	12.525945	12.340188	12.340136
		DQM	12.583171	12.525823	12.340131	12.340107
	01	NTM	10.978116	10.961978	10.437718	10.437645
		DQM	10.978005	10.961730	10.437576	10.437467

To gain deeper insight into the impact of the adsorption technique on the nonlocal frequencies of the adatom-microresonator, it is necessary to define a parameter that quantifies the corresponding frequency shift:

$$\Delta\omega^a = \frac{\omega^a_N - \omega^0_N}{\omega^0_N}. \tag{46}$$

The parameter $\Delta\omega_a$, referred to as the frequency shift ratio, serves as a critical metric for assessing variations in the dynamic performance due to the presence of adatoms. The parameter ω_0 denotes the nonlocal frequencies associated with a hollow microbeam in the absence of adsorbed atoms [35]. The Buckingham parameters [41], which are used in the computations, are shown in Table 2.

Table 2. Buckingham potential parameters used in vdW energy computations

Buckingham parameters	Pair	
	O^{2-}–O^{2-}	Si^{4+}–O^{2-}
A (eV)	1844.7458	13 702.905
ε (Å)	0.343645	0.193817
C (eV.Å^6)	192.58	54.681

The influence of adsorption density on the vibration behavior of the system is presented in Fig. 5 and its corresponding impact on the nonlocal frequency shift, using two distinct values for each parameter: the filling ratio α and number N.

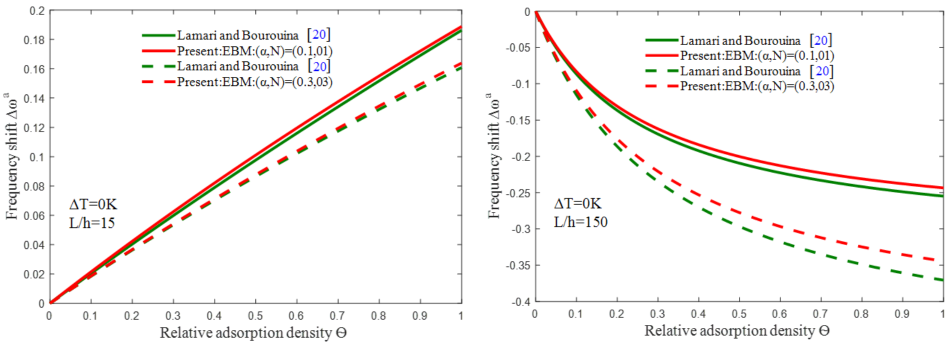

(a) (b)

Fig. 5. Validation comparison of the studied model for the current and previous works [22] at $\Delta T = 0$ K when: $L/h = 15$ (a); $L/h = 150$ (b)

Based on the EBM, a comparison is made between the numerical results obtained in the current study and those reported by [22] for validation of the studied model. The analysis is conducted for length-to-thickness ratios of $L/h = 15$ and $L/h = 150$, without thermal loading. The findings indicate that the decrease in frequency shift with increasing relative adsorption density θ is attributed to the increase in L/h ratio. Furthermore, the results exhibit excellent agreement with those reported by [51], thereby validating the accuracy and reliability of the proposed formulation and computational approach.

5.2. Parametric studies

Following the validation of the proposed formulation and numerical results, this subsection presents a series of parametric studies to examine the impact of key geometric parameters on the thermally induced performance of double FGPS microresonator. Utilizing both Euler and Rayleigh beam models, the impacts of the number of holes N, power-law index p, and porosity volume fraction ζ on the nonlocal frequency shift $\Delta\omega_N$ are analyzed for a double FGPS microresonator subjected to nonlinear thermal loading with evenly distributed:

$$\Delta\omega_N = \frac{(\omega_L - \omega_N)}{\omega_L}\,. \tag{47}$$

The nonlocal parameter μ ($\mu = ea/L$) plays an important role in nonlocal elasticity theory, as it incorporates an intrinsic material length scale and allows the model to account for small-scale effects that become significant at micro- and nanoscale dimensions [55]. Here, ω_L refers to the local frequency corresponding to the case where the nonlocal parameter μ is zero, while ω_N denotes the nonlocal frequency associated with a nonzero nonlocal parameter μ. The hole size ratio β (defined as $\beta = 1 - \alpha$) is a geometric parameter that quantifies the fraction of solid material replaced by holes within the microbeam [50]. A value of $\beta = 0$ corresponds to a fully solid microbeam, whereas $\beta = 1$ represents a completely hollow configuration [20]. Fig. 6 illustrates frequency shift behavior, obtained using RBM and EBM models, as a function of hole size ratio β (Fig. 6a and 6b) for three different values of both temperature change ΔT, power-law index p, and nonlocal parameter μ under nonlinear temperature load at coupling spring constant $k_{EM} = 0$ N/m for the single FGPS microresonator and at $k_{EM} = 10e4$ N/m for the double FGPS microresonators.

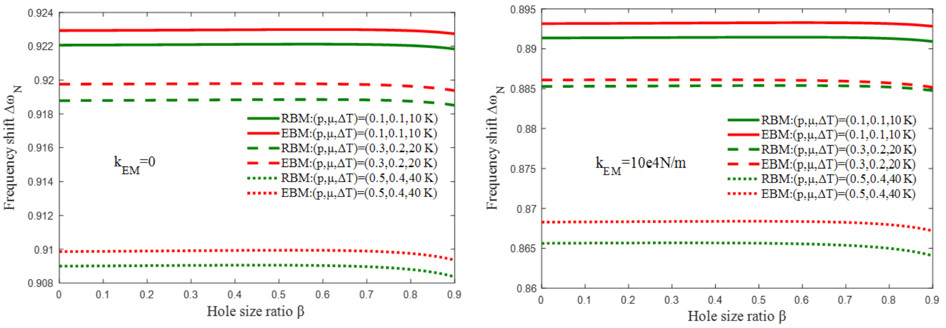

(a) (b)

Fig. 6. Nonlocal frequency shift versus hole size ratio β: $k_{EM} = 0$ (a), $k_{EM} = 10e4$ N/m (b) for different values of power-law index p, nonlocal scale parameter μ, and temperature change ΔT

A significant decrease in natural frequency change is detected upon incorporating the nonlocal parameter μ into the analysis for both the EBM and RBM, with a focus on the important influence of nonlocal elasticity in accurately characterizing the dynamic response of the functional system. Notably, the RBM nonlocal-induced frequency variation remains lower than the EBM frequency shift through the examined interval of hole size ratio β.

Fig. 7 shows that the computed frequency shift declines as the power-law index p rises in both models.

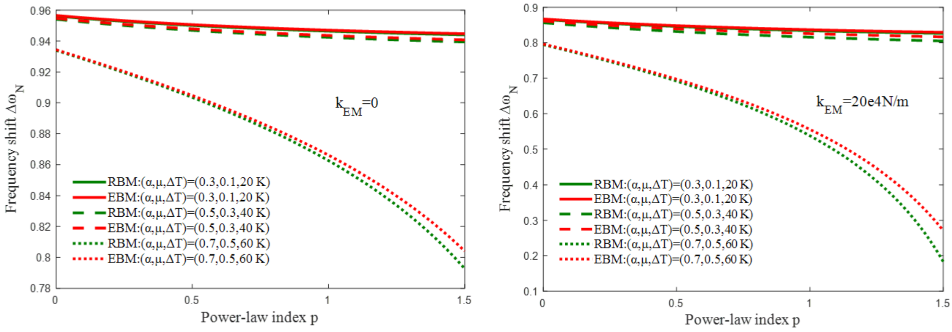

(a) (b)

Fig. 7. Nonlocal frequency shift versus power-law index p: $k_{EM} = 0$ (a), $k_{EM} = 20e4$ N/m (b) for different values of filling ratio α, nonlocal scale parameter μ, and temperature ΔT

Where, reflects a decrease in stiffness and dynamic behavior due to the varying distribution of FGM properties [19]. However, the rate of frequency shift reduction differs noticeably between the two models, particularly at higher values of the spring parameter k_{EM}. Notably, the EBM exhibits greater sensitivity to temperature change ΔT compared to the Rayleigh beam model. Both beam models show a clear variation in frequency as the number of holes N increases (Table 3).

Table 3. A comparison between the nonlocal frequencies [GHz] computed without and with applying the nonlinear thermal load using the analytical and numerical methods

N	μ	NTM/DQM	Double FGPS microbeams $\Delta T \neq 0$ K [Present]				Double FGPS microbeams $\Delta T = 0$ K [22]	
			Perfect ($\zeta = 0$)		Even ($\zeta = 0.5$)		Perfect ($\zeta = 0$)	Even ($\zeta = 0.5$)
			EBM	RBM	EBM	RBM	EBM	EBM
1	0.1	NTM	13.81985	13.81984	13.40145	13.40145	14.43774	13.48622
		DQM	13.81980	13.81972	13.40142	13.40142	14.43772	13.48621
	0.2	NTM	13.76827	13.76825	13.40051	13.40050	14.41576	13.45520
		DQM	13.76822	13.76813	13.40051	13.40015	14.41562	13.45507
2	0.1	NTM	13.64149	13.64138	12.43137	12.43127	13.75886	12.48343
		DQM	13.64143	13.64133	12.43132	12.43122	13.75866	12.48328
	0.2	NTM	13.60262	13.60261	12.40585	12.40563	13.73522	12.44886
		DQM	13.60261	13.60248	12.40583	12.40524	13.73521	12.44884

Fig. 8 demonstrates the combined influence of perforation geometry parameters, elastic medium coupling k_{EM}, and nonlinear thermal loading on the vibration of double FGPS microresonators. Where, represents the variation of nonlocal frequency ω_N as a function of the filling ratio α and the number of holes N under two different elastic medium stiffness conditions $k_{EM} = 0$ (Fig. 8a), and $k_{EM} = 10e4$ N/m (Fig. 8b), for two temperature change values $\Delta T = 30$ K and

ΔT = 50 K. Both the EBM and the RBM are compared to focus on the influence of rotary inertia and thermal effects on the dynamic response. In Fig. 8 (a and b), the upper surface corresponds to the EBM, and the lower surface represents the RBM.

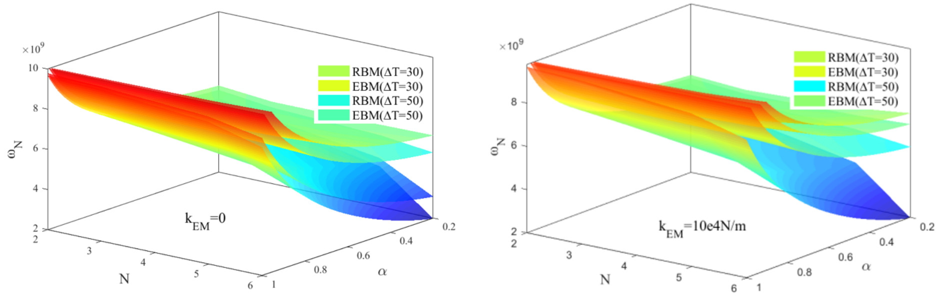

(a) (b)

Fig. 8. Nonlocal frequency [Hz] versus filling ratio α and holes number N at different values of temperature change ΔT for EBM upper surface and RBM lower surface: k_{EM} = 0 (a), k_{EM} = 10e4 N/m (b)

In both cases, increasing the filling ratio α results in a noticeable increase in the nonlocal frequency ω_N, especially at the lowest hole numbers N. This trend is consistent with the results in Refs [19, 49]. The inclusion of the elastic medium stiffness k_{EM} noticeably elevates the frequency values, indicating that the coupling stiffness acts as an additional constraint that enhances the equivalent stiffness of the system [11].

Regarding the temperature change ΔT, an increase from 30 to 50 K amplifies the frequency softening effect, particularly for the RBM. This can be attributed to the thermally induced softening of material properties, where thermal stresses reduce the effective stiffness of the microresonator. The difference between the two beam models becomes more pronounced under higher thermal loads.

5.3. Nonlinear effects of temperature change

The vibration performance of a double FGPS microresonator with distributed oxygen charge on its surface was analyzed and subjected to nonlinear thermal load. To examine the influence of nonlinear thermal load on the system's dynamic response, the computations of frequency shift were carried out using a ratio as follows:

$$\Delta\omega_T = \frac{(\omega_T - \omega_0)}{\omega_T}, \tag{48}$$

where ω_T represents the nonlocal frequency of the system under nonlinear thermal load, ω_0 represents the nonlocal frequency without the nonlinear thermal load effect. The results in Fig. 9 show that the dimensionless frequency shift as a function of the temperature change ΔT decreases noticeably as the porosity volume fraction

ζ increases, with the reduction becoming particularly pronounced at higher values of the porosity volume fraction ζ [22]. At low porosity ($p = 0.2$) without elastic coupling, the system shows larger frequency shifts and clear differences between the Euler and Rayleigh beam models [10]. In contrast, at high porosity ($p = 0.8$) with strong elastic medium coupling, the total frequency shift is reduced, and the differences between models narrow, indicating that coupling stiffness suppresses dynamic sensitivity [7]. On the other hand, the frequency shift shows a distinctive non-monotonic trend; it initially decreases slightly as ΔT increases and then sharply rises beyond a certain thermal threshold.

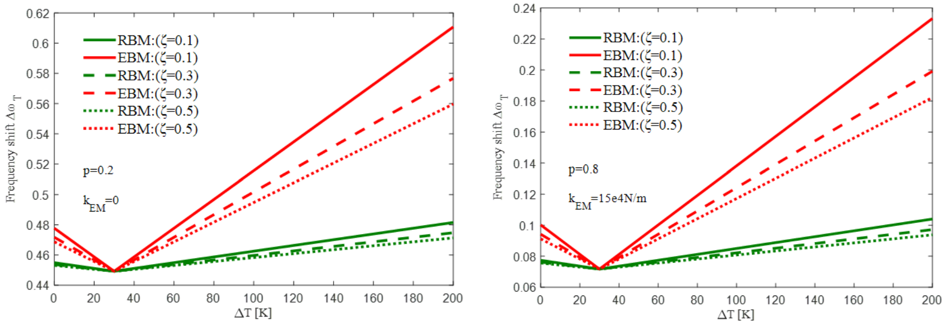

(a) (b)

Fig. 9. Nonlocal frequency shift versus the temperature change ΔT for three values of ζ with: $p = 0.2$, $k_{EM} = 0$ (a); $p = 0.8$, $k_{EM} = 15e4$ N/m (b)

Table 4 presents the computed values of the nonlocal frequency ω_T for a double FGPS microresonator operating under a nonlinear thermal environment. The frequencies are calculated for temperature changes $\Delta T = 0$, 30, and 60 K, with nonlocal parameters $\mu = 0.2$, 0.4 and 0.6, and power-law indices $p = 0.3$ and 0.7.

Table 4. Nonlocal frequency [GHz] computed by the analytical and numerical methods for different values of the temperature change

μ	p	NTM/DQM	$\Delta T = 0$ [K]		$\Delta T = 30$ [K]		$\Delta T = 60$ [K]	
			EBM	RBM	EBM	RBM	EBM	RBM
0.2	0.3	NTM	17.41448	17.41448	17.38852	17.38852	17.40034	17.35236
		DQM	17.41446	17.41445	17.38839	17.38838	17.40019	17.35232
	0.7	NTM	16.19144	16.19143	16.16597	16.16597	16.14236	16.10782
		DQM	16.19142	16.19131	16.16582	16.16582	16.14221	16.10767
0.4	0.3	NTM	17.22195	17.22195	17.20918	17.20917	17.19664	17.13026
		DQM	17.22192	17.22172	17.20913	17.20914	17.19648	17.13024
	0.7	NTM	15.93498	15.93498	15.91311	15.91311	15.88870	15.86056
		DQM	15.93491	15.93482	15.91310	15.91310	15.88856	15.86041

The results indicate that the frequency ω_T decreases as the power-law index p, nonlocal parameter μ, and temperature change ΔT increase, demonstrating an inverse relationship with these parameters [56].

Fig. 10 presents the nonlocal frequency ω_T concerning the nonlocal parameter μ and the distributed oxygen charge density Θ, under two thermal change values ($\Delta T = 30$ K) and ($\Delta T = 50$ K) for both EBM and RBM beam models, where the upper surface corresponds to the EBM, while the lower surface represents the RBM. The results show that increasing the nonlocal parameter μ leads to a consistent reduction in the nonlocal frequency for both models, reflecting the softening effect due to small-scale phenomena. This decrease is more significant in the RBM due to the inclusion of rotary inertia, which further enhances structural flexibility [56].

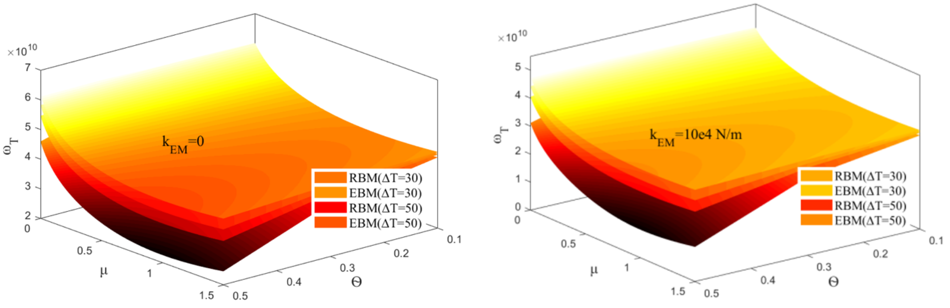

(a) (b)

Fig. 10. Nonlocal frequency [Hz] versus nonlocal parameter μ and adsorption density Θ at two values of temperature change ΔT for EBM upper surface and RBM lower surface: $k_{EM} = 0$ (a), $k_{EM} = 10e4$ N/m (b)

Additionally, the distributed oxygen charge density Θ, also contributes to lowering the frequency as it adds mass (from ρA_{eq} to $\rho A_{\text{eq}} + \eta b m_O^-$) to the system and reduces stiffness [7]. The influence of thermal effects becomes more pronounced at higher temperature changes, as seen for $\Delta T = 50$ K, where the drop in frequency is more substantial compared to $\Delta T = 30$ K.

6. Conclusions

The nonlocal vibration of an adatom-functionalized resonator incorporating a hollow microcore was examined under the influence of a nonlinear thermal field and the distributed oxygen charge on the effective surface of the system. The analysis was carried out within the framework of the NSGT, and frequency shifts were determined for both the EBM and RBM by integrating vdW interactions using the Buckingham-Coulomb potential formulation. Key conclusions derived through both the NTS and DQM are outlined below:

- The developed models successfully capture the microresonator's total bending behavior, indicating that adsorbed atoms significantly decrease the dynamic frequency due to their added mass and interaction energy.
- The RBM consistently predicts lower frequency values than the EBM counterpart, primarily because of rotary inertia effects.
- The resonance behavior of the double FGPS microresonator is notably impacted by variations in thermal gradients, suggesting the importance of thermal field control in system design.
- Small-scale phenomena, emphasized by the nonlocal parameter μ and elastic medium constant k_{EM}, were found to increase the mechanical compliance of the system, especially when a hollow core is incorporated, thereby boosting the flexibility of the structure.
- Tailoring the porosity profile across the microbeam layers contributes to a decrease in the system's equivalent mass, enhancing the dynamic responsiveness and improving the total efficiency of the microresonator.

The presented approach offers a comprehensive multiphysical modeling strategy for adatom-interfaced microresonator systems. The findings advance the understanding of microscale interaction mechanisms and provide useful guidance for designing responsive, high-performance devices suited for thermal sensing and precision microengineering applications.

References

[1] O. Mazur and J. Awrejcewicz. The nonlocal elasticity theory for geometrically nonlinear vibrations of double-layer nanoplate systems in magnetic field. *Meccanica*, 57:2835–2847, 2022. doi: 10.1007/s11012-022-01602-9.

[2] V.C. Nguyen, M.H. Chu, M.C. Bui, and V.D. Nguyen. One-axis micro-electromechanical accelerometer with enhanced sensitivity. *Archive of Mechanical Engineering*, 72(2):311–332, 2025. doi: 10.24425/ame.2025.154738.

[3] A.H. Ghorbanpour-Arani, A. Rastgoo, M.M. Sharafi, R. Kolahchi, and A. GhorbanpourArani. Nonlocal viscoelasticity based vibration of double viscoelastic piezoelectric nanobeam systems. *Meccanica*, 51:25–40, 2016. doi: 10.1007/s11012-014-9991-0.

[4] S. Kumar. Dynamic behaviour of axially functionally graded beam resting on variable elastic foundation. *Archive of Mechanical Engineering*, 67(4):451–470, 2020. doi: 10.24425/ame.2020.131700.

[5] M. Coleman and L. McSweeney. The exact frequency equations for the Rayleigh and shear beams with boundary damping. *International Journal of Acoustics and Vibration*, 25:3–8, 2020. doi: 10.20855/ijav.2020.25.11422.

[6] T. Elaikh, N. Abd, and A.H. Ali. Dynamic characteristics of cracked simply supported bidirectional functionally graded Rayleigh beam. *Results in Materials*, 19:100441, 2023. doi: 10.1016/j.rinma.2023.100441.

[7] A. Lamari, H. Bourouina, S. Khouni, Y. Maiza, and M. Mektout. Double functionally graded porous resonator combining hollow microcore via nonlocal strain gradient approach for large adsorption of water molecules. *International Journal of Mechanics and Materials in Design*, July 2025. doi: 10.1007/s10999-025-09797-x.

[8] M. Mektout, H. Bourouina, Y. Maiza, S. Khouni, A. Lamari, B.S. Djellali, and L. Elaihar. Functional resonator-based nonlocal FGP hollow adsorber for wide detection of coupled biomolecules using DQM framework. *Meccanica*, 2025. doi: 10.1007/s11012-025-02025-y.

[9] I. Esen. Dynamic response of functionally graded Timoshenko beams in a thermal environment subjected to an accelerating load. *European Journal of Mechanics - A/Solids*, 78:103841, 2019. doi: 10.1016/j.euromechsol.2019.103841.

[10] S. Adali. Variational principles for a double Rayleigh beam system undergoing vibrations and connected by a nonlinear Winkler–Pasternak elastic layer. *Nonlinear Engineering*, 12:1, 2023. doi: 10.1515/nleng-2022-0259.

[11] H. Bourouina, N. Derguini, and R. Yahiaoui. Coupling spring-induced resonance shift in PDNB system with PSH network. *Microsystem Technologies*, 29:91–106, 2023. doi: 10.1007/s00542-022-05393-7.

[12] Z. Liu, G. Wang, J. Zhang, X. Rui, L. Gu, and X. Zhang. A systematic method for free and forced vibration analysis of axially loaded hybrid double-beam systems. *Meccanica*, 2025. doi: 10.1007/s11012-025-02026-x.

[13] M.A. Hamed, M.A. Eltaher, A.M. Sadoun, and K.H. Almitani. Free vibration of symmetric and sigmoid functionally graded nanobeams. *Applied Physics A*, 122:829, 2016. doi: 10.1007/s00339-016-0324-0.

[14] M. Hemmatnezhad and M. Javid. Finite element formulation for the large-amplitude vibrations of FG beams. *Archive of Mechanical Engineering*, 61(3):469–482, 2014. doi: 10.2478/meceng-2014-0027.

[15] M. Avcar and H.H.A. Alwan. Free vibration of functionally graded Rayleigh beam. *International Journal of Engineering and Applied Sciences*, 9:Article 2, 2017. doi: 10.24107/ijeas.322884.

[16] T.Q. Hung, D.M. Duc, and T.M. Tu. Free vibration analysis of sandwich beam with porous FGM core in thermal environment using mesh-free approach. *Archive of Mechanical Engineering*, 69(3):471–496, 2022. doi: 10.24425/ame.2022.140422.

[17] I. Baghdali, A. Attia, F. Bourada, A.A. Bousahla, A. Tounsi, H. Heireche, A. Tounsi, M. Bourada, and M. Yaylaci. Analysis of the impact of the viscoelastic foundation on bending and vibration of FG porous nanoplates within integral higher-order shear deformation theory. *Physical Mesomechanics*, 28:245–262, 2025. doi: 10.1134/S1029959924601313.

[18] M. Arefi, M. Kiani, and O. Civalek. 3-D magneto-electro-thermal analysis of layered nanoplate including porous core nanoplate and piezomagnetic face-sheets. *Applied Physics A*, 126:76, 2020. doi: 10.1007/s00339-019-3241-1.

[19] Y. Maiza and H. Bourouina. Non-local response prediction for FGP sandwich microbeam with 2D PSH network subjected to adatoms-substrate interactions and excited by magnetic intensity. *Acta Mechanica*, 236:259–288, 2025. doi: 10.1007/s00707-024-04149-w.

[20] A. Abdelrahman and M.A. Eltaher. On bending and buckling responses of perforated nanobeams including surface energy for different beam theories. *Engineering with Computers*, 38:1–27, 2022. doi: 10.1007/s00366-020-01211-8.

[21] Ö. Civalek, B. Uzun, and M. Ö. Yaylı. Size-dependent nonlinear stability response of perforated nano/microbeams via Fourier series. *Archive of Applied Mechanics*, 93:4425–4443, 2023. doi: 10.1007/s00419-023-02501-5.

[22] A. Lamari and H. Bourouina. Nonlocal vibration response of double FG porous microbeamsadsorber with 2D PSH network under magnetic intensity for large frequency range. *Journal of Vibration Engineering & Technologies*, 13:38, 2025. doi: 10.1007/s42417-024-01571-1.

[23] U. Kafkas. On the free vibration of a perforated Rayleigh beam with deformable ends. *Engineering Science and Technology, an International Journal*, 56:101787, 2024. doi: 10.1016/j.jestch.2024.101787.

[24] T. Merzouki and M.S.A. Houari. Nonlocal strain gradient theory for free vibration analysis of FG nano-scale beams in thermal environments using an efficient numerical model. *Journal of Vibration Engineering & Technologies*, 12:8775–8800, 2024. doi: 10.1007/s42417-024-01389-x.

[25] A.M. Zenkour and A.F. Radwan. A nonlocal strain gradient theory for porous functionally graded curved nanobeams under different boundary conditions. *Physical Mesomechanics*, 23:601–615, 2020. doi: 10.1134/S1029959920060168.

[26] A.A. Abdelrahman, I. Esen, C. Özarpa, and M.A. Eltaher. Dynamics of perforated nanobeams subject to moving mass using the nonlocal strain gradient theory. *Applied Mathematical Modelling*, 96:215–235, 2021. doi: 10.1016/j.apm.2021.03.008.

[27] P. Sourani, M. Hashemian, M. Pirmoradian, and D. Toghraie. A comparison of the Bolotin and incremental harmonic balance methods in the dynamic stability analysis of an Euler–Bernoulli nanobeam based on the non-local strain gradient theory and surface effects. *Mechanics of Materials*, 145:103403, 2020. doi: 10.1016/j.mechmat.2020.103403.

[28] M. Guerroudj et al. Size-dependent free vibration analysis of multidirectional functionally graded nanobeams via a nonlocal strain gradient theory. *Journal of Engineering Mathematics*, 146:20, 2024. doi: 10.1007/s10665-024-10373-z.

[29] V.V. Vasiliev and S.A. Lurie. On correct nonlocal generalized theories of elasticity. *Physical Mesomechanics*, 19:269–281, 2016. doi: 10.1134/S102995991603005X.

[30] I. Bensaid, A. Saimi, A. Cheikh, H. AitAtmane, M. Dahmane, and H. Assem. Vibration and buckling analysis of quasi-3D porous composite steel-polymer concrete box section beams via DQFEM. *Archive of Mechanical Engineering*, 72(2):271–292, 2025. doi: 10.24425/ame.2025.154737.

[31] M. Feri, A. Alibeigloo, and A.A. Pasha Zanoosi. Three-dimensional static and free vibration analysis of cross-ply laminated plate bonded with piezoelectric layers using differential quadrature method. *Meccanica*, 51:1723–1740, 2016. doi: 10.1007/s11012-015-0246-5.

[32] M. Karimi and A.R. Shahidi. Comparing magnitudes of surface energy stress in synchronous and asynchronous bending/buckling analysis of slanting double-layer METE nanoplates. *Applied Physics A*, 125:154, 2019. doi: 10.1007/s00339-019-2429-8.

[33] R. Selvamani, L. Rubine, T. Prabhakaran, and M. Yaylaci. Free vibration analysis of a functionally graded magneto-piezo-thermoelastic ceramic-metal nanobeam using modified nonlocal state-space strain gradient theory. *Physical Mesomechanics*, 28:263–274, 2025. doi: 10.1134/S1029959924601258.

[34] V.L. Nguyen, M.T. Tran, V.L. Nguyen, and Q.H. Le. Static behaviour of functionally graded plates resting on elastic foundations using neutral surface concept. *Archive of Mechanical Engineering*, 68(1):5–22, 2021. doi: 10.24425/ame.2020.131706.

[35] H. Bourouina, et al. The influence of hole networks on the adsorption-induced frequency shift of a perforated nanobeam using non-local elasticity theory. *Journal of Physics and Chemistry of Solids*, 136:109201, 2020. doi: 10.1016/j.jpcs.2019.109201.

[36] L. Elaihar, H. Bourouina, S. Khouni, B.S. Djellali, A. Lamari, Y. Maiza, and M. Mektout. Adaptive framework for FGPS bio-resonators with hollow microcore for mass detection combining nonlocal DQM computation. *Acta Mechanica*, 236:4655–4697, 2025. doi: 10.1007/s00707-025-04403-9.

[37] S. Khouni and H. Bourouina. Nonlocal FG porous adsorber with 2D PSH network under magnetic intensity for large frequency range considering vdW interaction potentials. *Physica Scripta*, 99:105919, 2024. doi: 10.1088/1402-4896/ad72b5.

[38] M. Ghommem and A. Abdelkefi. Nonlinear reduced-order modeling and effectiveness of electrically-actuated microbeams for bio-mass sensing applications. *International Journal of Mechanics and Materials in Design*, 15:125–143, 2019. doi: 10.1007/s10999-018-9402-0.

[39] H. Bourouina and A. Boussendel. Theoretical prediction of proteins network-induced nonlocal response in molecules–resonator biosensor with hydrogen bonds including van der Waals interactions. *PhysicaScripta*, 99:115012, 2024. doi: 10.1088/1402-4896/ad23af.

[40] J.Q. Zhang, X.Q. Feng, and G.Y. Huang. Chemisorption-induced resonance frequency shift of a microcantilever. *Chinese Physics Letters*, 29(5):056801, 2012. doi: 10.1088/0256-307X/29/5/056801.

[41] K. Okhotnikov, B. Stevensson, and M. Edén. New interatomic potential parameters for molecular dynamics simulations of rare-earth (RE = La, Y, Lu, Sc) aluminosilicate glass structures: exploration of RE^{3+} field-strength effects. *Physical Chemistry Chemical Physics*, 15(36):15041–15055, 2013. doi: 10.1039/C3CP51726H.

[42] P. Shukla, A. Chernatynskiy, J.C. Nino, S.B. Sinnott, and S.R. Phillpot. Effect of inversion on thermoelastic and thermal transport properties of MgAl2O4 spinel by atomistic simulation. *Journal of Materials Science*, 46:55–62, 2011. doi: 10.1007/s10853-010-4795-7.

[43] A.A. Hassanali and S.J. Singer. Static and dynamic properties of the water/amorphous silica interface: a model for the undissociated surface. *Journal of Computer-Aided Materials Design*, 14:53–63, 2007. doi: 10.1007/s10820-006-9038-5.

[44] W.R. Chen, H. Chang, and C.S. Chen. Thermal buckling of temperature-dependent functionally graded Timoshenko beams. *Archive of Mechanical Engineering*, 66(4):393–415, 2019. doi: 10.24425/ame.2019.131354.

[45] S. Abdelbari, A. Attia, F. Bourada, A.A. Bousahla, A. Tounsi, and M.H. Ghazwani. Investigation of dynamic characteristics of imperfect FG beams on the Winkler–Pasternak foundation under thermal loading. *Physical Mesomechanics*, 26(5):557–572, 2023. doi: 10.1134/S1029959923050089.

[46] A. Rahmani, I. Ahmadi, and A. Babaei. Transverse vibration analysis of nonlocal beams with various slenderness ratios, undergoing thermal stress. *Archive of Mechanical Engineering*, 66(1):5–24, 2019. doi: 10.24425/ame.2019.126368.

[47] E. Salari, S.A. SadoughVanini, A.R. Ashoori, and A.H. Akbarzadeh. Nonlinear thermal behavior of shear deformable FG porous nanobeams with geometrical imperfection: Snap-through and postbuckling analysis. *International Journal of Mechanical Sciences*, 178:105615, 2020. doi: 10.1016/j.ijmecsci.2020.105615.

[48] N. Wattanasakulpong and V. Ungbhakorn. Linear and nonlinear vibration analysis of elastically restrained ends FGM beams with porosities. *Aerospace Science and Technology*, 32(1):111–120, 2014. doi: 10.1016/j.ast.2013.12.002.

[49] L. Luschi and F. Pieri. An analytical model for the resonance frequency of square perforated Lamé-mode resonators. *Sensors and Actuators B: Chemical*, 222:1233–1239, 2016. doi: 10.1016/j.snb.2015.07.085.

[50] H. Bourouina, R. Yahiaoui, A. Sahar, and M.E.A. Benamar. Analytical modeling for the determination of nonlocal resonance frequencies of perforated nanobeams subjected to temperature-induced loads. *Physica E: Low-Dimensional Systems and Nanostructures*, 75:163–168, 2016. doi: 10.1016/j.physe.2015.09.014.

[51] B. Gheshlaghi and S. Hasheminejad. Adsorption-induced resonance frequency shift in Timoshenko microbeams. *Current Applied Physics*, 11:1035–1041, 2011. doi: 10.1016/j.cap.2011.01.025.

[52] X. Xu and Z. Deng. Surface effects of adsorption-induced resonance analysis on micro/-nanobeams via nonlocal elasticity. *Applied Mathematics and Mechanics (English Edition)*, 34:37–44, 2013. doi: 10.1007/s10483-013-1651-9.

[53] M.A. Attia, M.S. Matbuly, T. Osman, and M. AbdElkhalek. Dynamic analysis of double cracked bi-directional functionally graded nanobeam using the differential quadrature method. *Acta Mechanica*, 235:1961–2012, 2024. doi: 10.1007/s00707-023-03797-8.

[54] A.R. Kermany, J.S. Bennett, V.M. Valenzuela, W.P. Bowen, and F. Iacopi. Potential of epitaxial silicon carbide microbeam resonators for chemical sensing. *Physica Status Solidi A*, 214:1600437, 2017. doi: 10.1002/pssa.201600437.

[55] C.W. Lim, G. Zhang, and J.N. Reddy. A higher-order nonlocal elasticity and strain gradient theory and its applications in wave propagation. *Journal of the Mechanics and Physics of Solids*, 78:298–313, 2015. doi: 10.1016/j.jmps.2015.02.001.

[56] F. Pehlivan, I. Esen, and K.G. Aktas. Thermomechanical response of smart magneto-electro-elastic FGM nanosensor beams with intended porosity. *Arabian Journal for Science and Engineering*, 50:2755–2777, 2025. doi: 10.1007/s13369-024-09197-x.